Kinematic analysis of a 5-DOF hybrid-driven MR compatible robot for minimally invasive prostatic interventions

Shan Jiang†*, Jie Guo†, Shen Liu†, Jun Liu‡ and Jun Yang‡

†*School of Mechanical Engineering, Tianjin University, Tianjin, China*
‡*Department of Magnetic Resonance, Tianjin Union Medicine Centre, Tianjin, China*

SUMMARY

This paper introduces the design and kinematic analysis of a 5-DOF (multiple degree of freedom) hybrid-driven MR (Magnetic Resonance) compatible robot for prostate brachytherapy. It can slip the leash of template and rely on the high precise of MR imaging. After a brief introduction on design requirements of MR compatible robot, a description of our robot structure, material selection, hybrid-driven, and control architecture are presented. Secondly, the forward kinematics equations are obtained according to the equivalent diagram of this robot, and the actual workspace can be outlined. This will help the designer to determine whether this robot can be operated in the MR core without intervention with patient. And then, the inverse kinematics equations combined with trajectory planning are used to calculate the actuators movement. This will help the control system to manipulate the robotic accurately. Finally, vision based experiments on phantoms are used to verify the mechanism precision . As the results shown, the needle tip precision of mechanism is 0.9 mm in the general lab environment.

KEYWORDS: Hybrid-driven; Needle insertion; Forward kinematics; Inverse kinematics; MR compatible robot.

1. Introduction

Prostate cancer is a major health problem for men, which alone accounts for 25% (192,280) of incident cases of cancer in men of United States, 2009.[1] Brachytherapy, which is currently considered to be an effective radiation therapy used to treat cancer, is a process of implanting some radioactivity seeds to kill the cancers without serious side effects. In this treatment procedure, needle insertion is a main solution to perform this brachytherapy. About 60–100 radioactive seeds are implanted by a slender needle which is about 120–150 mm long.[2] However, the traditional means of implanting seed at planned position is challenging due to a variety of reasons. In the process of manual insertion, the needle penetrates into the skin assisted by a fixed guiding template that is used to orient the needle along a grid of horizontal holes. It only allows the needle inserting at horizontal direction and constrains needle from pitch and yaw. Although the target position is commonly along the lines at the horizontal direction, it deviates from the original

location due to tissue deformation caused by needle-tissue interaction.[3] Assisted by a multiple degree of freedom (DOF) robot, brachytherapy can be conducted without template and the needle can be oriented during the process of insertion.[4] In the recent brachytherapy research, a directional radioactive seed is designed to be partially shielded, thus, it does not emit radiation in all directions. In order that the radiation source can be oriented to irradiate cancerous tissues while sparing normal ones, the placement of the sources necessitates a new, highly accurate method for localization in 6 DOF. A robot is the best way to accomplish this task accurately.[5,6]

Another disadvantage that brings placement errors during this treatment is the manual insertion unsteadily. If insertion manually during the surgery, hand trembling will be enlarged by the long and thin needle and results in the implant imprecisely. This is usually happened when the surgeon is less skilled or inexperienced. And, current methods do not easily meet spatial and stable positioning requirements.[7] Therefore, needle insertion with robot assistance could improve the stability and precision of the surgery.

Along with the development of Magnetic Resonance (MR) and Computed Tomography (CT) technology, image guided minimally invasive surgery assisted by the robot has brought tremendous change in medical application. As in soft tissue surgery, such as brachytherapy, biopsy, soft tissue will deform in large scale for the needle-tissue force interaction. According to the real time image information feedback, controller can manipulate the robot to adjust the insertion depth and orientation. All in all, robot assist brachytherapy with real-time imaging can not only improve the precision and correctness of the surgery but also result in less pain and scarring, reduced blood loss and transfusions, lower risk of complication, shorter hospital stays, and faster recovery periods.[8]

For such merits mentioned above, brachytherapy assisted by robot has been proposed by many investigators. According to the image guided fashion robot assist brahcytherapy can be divided into CT guided, Transrectal Ultrasound (TRUS) guided, and MRI guided system.[9] D. Liu, et al.[10] presented a hybrid robot system for CT-guided surgery and the locating precision of the hybid robot reaches 1.08 mm. Q. Huang, et al.[11] introduced an 5-DOF robotic system for microwave ablation of liver cancer with 2D ultrasound guided. H. Bassan, et al.[12] built a 5-DOF hybrid robotic system to perform 3D ultrasound guided percutaneous needle insertion surgery. A macro–micro system was adopted in the

* Corresponding author. E-mail: shanjiang@tju.edu.cn

design of the robot. The macro stage is responsible for the orientation of the needle with parallel mechanism and the micro stage for needle insertion and rotation. S. E. Salcudean *et al.*[13] introduced a 4-DOF serial robot for prostate needle orientation and 2 DOF for needle insertion and rotation with ultrasound imaging guidance. Yu. Y *et al.*[14] presented a 16-DOF TRUS guided robot system that comprised of a 9-DOF positioning module and a 7-DOF surgery module. The system used for prostate brachytherapy can be operated automatically and semi-automatically. Force sensors and optical encoders were incorporated into the prototype to improve the needle insertion accuracy. PVC (poly vinyl chloride) phantom experiment were carried out to assess the implant accuracy is 0.67 mm in *x* direction, 0.13 mm in *y* direction, and 0.11 mm in *z* direction.

TRUS image guided surgery is an easy and convenient method used in clinical therapy. It doesn't need special material and actuate method for the robot. However, it is not accurate for tumor localization, and therefore precludes the precise identification and sampling of individual cancerous tumor sites.[15] Advance MR technology development affords images with higher anatomical resolution and contrast that can be obtained with TRUS.[4] Therefore, MRI guided robot assist brachytherapy system has been investigated in large scale. Nevertheless, robot operating in the high magnetic field and limited workspace has been challenging the designer all the while.

A new MRI guided robot system MRI-P for prostatic intervention has been built by Godenberg *et al.*[9] MRI-P has 5 DOF. Through a modular trocar, surgical tool can be mounted on the robot and different kinds of surgery can be conducted. The robot accuracy assessment, MR compatible, image visualization, and thermal mapping on phantoms had been tested in MR core. The needle tip position error is less than 1.2 mm. Stoianovici[16] developed a pneumatically actuated robot for prostate interventions based on a newly invented pneumatic motor; and G. S. Fischer *et al.*[17] introduced a 4-DOF hybrid robot for real-time control transperineal prostate needle orientation under MRI guidance and perform insertion motion manually. Aiming at the special characteristic of needle insertion, the robot generally consisted of two parts: one for needle orientation, and the other for needle insertion. The main part for orientation must support the upper stage for insertion with enough loading capacity. And the slave part is responsible for needle insertion with compact structure and stable, flexible and precise movement. However, pneumatically actuated robots have shown the minimum distraction in the environment, but the confined workspace limits optimal robot design and thus controllability is often poor. Sang E Song *et al.*[18] reported that using external damping mechanism and timing belts on a 4-DOF parallel robot can improve the robot positioning accuracy.

In this paper, the mechanism design of a 5-DOF robot and its hybrid-driven control system architecture are introduced firstly. In Section 3, kinematic analysis of the robot structure is deduced and workspace is calculated. Through inverse kinematics analysis, the control parameters are achieved. The trajectory planning and a further kinematic simulation on inverse solution are presented in Section 4. Section 5 is
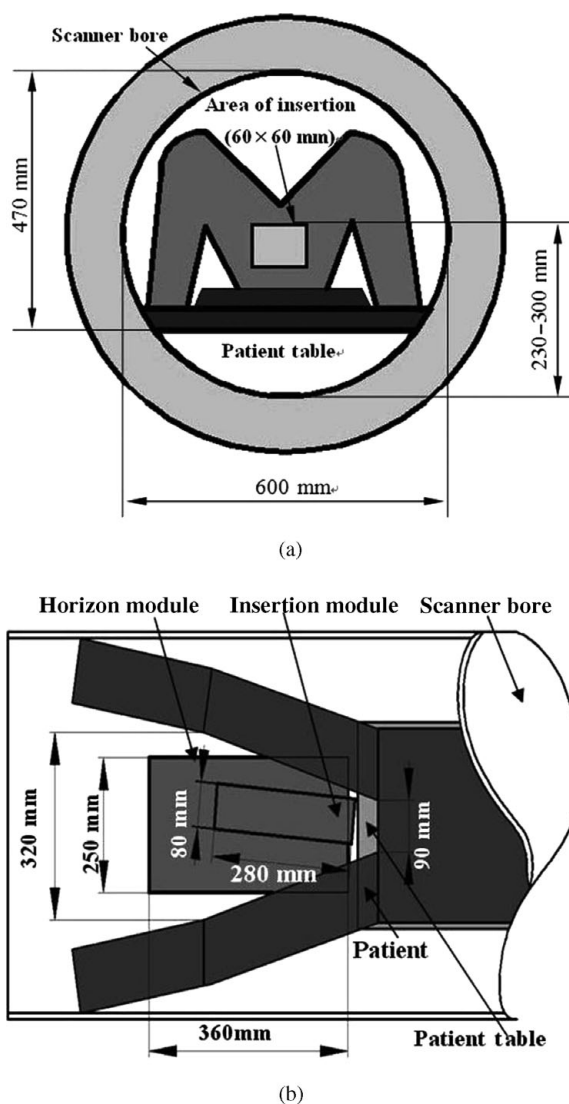

(a)

(b)

Fig. 1. Workspace for prostate brachytherapy in MRI bore.

dedicated to the experiment validation. And the last section is devoted to the discussion and the future work.

2. Description of Robot

2.1. Design requirements

Robot assist prostate brachytherapy is the surgery that performed by the robot with remote control other than the surgeon access to the patient. In this research patient is supposed in the supine position in the MR core. The magnetic field is 1.5 T. So, the design requirements can be concluded as following:

- The material, actuators, and sensors of the robotic system must be MR-compatible. The robotic system must not disturb magnetic field and bring distortion to image. MRI devices should not create a disturbance on performance of the robotic system and hurt the patient.
- As the robot should be operated between the patient legs, and the patient is in supine position in MR. The size and motion range of robot are confined to a limited workspace as shown in Fig. 1(a) and (b). During the operation, as
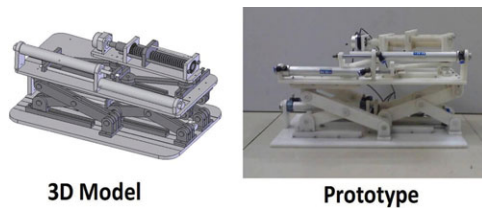
Fig. 2. (Colour online) 3D model and prototype of robot.

the patient's legs will be held up, the bottom of the robot is permitted to be slightly bigger than the top structure. However, since the insertion module that at the top of the robot is responsible for needle motion and will be oriented between two legs, so, a strictly compact structure is proposed.

- Brachytherapy needs the seeds should be implanted in the gland with higher accuracy, consistency and efficiency. Robot that substitute for the manual operation should have a placement error less than 2 mm that is generally considered acceptable (or desirable) clinically.[14]

2.2. Robot prototype

To perform the surgery in MRI bore, the robot cannot be built with any ferromagnetic material. In this research, polyformaldehyde (POM) is chosen for its magnetic inertial.

Robots used in serial structure have some advantages, such as bigger workspace, flexible movement, *et al.* Parallel mechanism that has unique advantages in other aspects, such as lower inertial, large load capacity, high stiffness, high acceleration *et al.* Respect to surgery requirements, a hybrid structures with the advantages of parallel and serial mechanism is adopted in this research. As shown in Fig. 2, 3D model and a prototype of the robot are built. The robot is comprised of three stages: the pitch/lift module, the yaw/horizontal module, and the insertion module. The former two stages at bottom and in mid assembled by serial structure are responsible for needle orientation. Each of stage adopts a pair of slider-guide mechanism with hybrid structure to perform translation and rotation motions. The joints between the bottom and middle stage contain four connection points: two of them are hinges and the other two are slipper guides. Similarly, two joints with one hinged point and one slipper guide are adopted between the top stage and the middle stage. The cooperation of the stages can produce lift, pitch, yaw, and horizontal motion to orient the needle tip at the position for insertion. The insertion module at top is to perform needle insertion with screw structure. Hence, the whole system can be considered as a serial-parallel mechanism, which possesses the advantages of both the serial mechanism (with a larger workspace) and the parallel mechanism (with a higher stiffness).

Dimension of the robot is about 450 mm in length 200 mm in width and 200 mm in height. The weight is about 9 kg. Horizontal translation is 100 mm; vertical translation is 150 mm; pitch angle is −16°; yaw angle is −15°. Additionally, to maintain the robot at the desired position to insert,

rod locks are needed to lock the cylinder rod. The MRI compatible pneumatic rod locks is developed.

2.3. Actuate and Control system architecture

To fulfill the requirement of MR compatible, four pneumatic cylinders and one ultrasonic motor are used to drive the robot. At the stages of insertion module orientation, pneumatic cylinders can offer high speed and large power density, which allow the bottom of the robotic system to remain steady with a heavy load. At the stage of needle insertion, a Piezotech PUMR40 (Piezo Electric Technology Co., Ltd) ultrasound motor is used for its low speed, high torque, compact size, and quick response. Optical encoder is chosen as the position sensor. The MR318 ZAPFREE fiber optic rotary encoder of Micronor that is fully MRI compatible is based on this approach. Combined with MR310 REI Module of Micronor, the electric signal that will be sent to the controller is acquired. Four MR318 encoders and MR310 modules are adopted in our robot, to measure the angle of each slider-guide mechanism.

As shown in Fig. 3, tumor position is acquired from MRI recognition. Through the inverse kinematics analysis, parameters such as pistons motion range and ultrasonic motor control parameters can be achieved. As the robot is hybrid actuated by pneumatic cylinder and ultrasonic motor, the control of the robot consisted of mainly two parts: low-level controllers that manage the control of pneumatic cylinders and the ultrasonic motor. High-level controller computes the references for the low-level controllers and coordinates their action. A controller based on high frequency valves using fuzzy PWM method has been developed in this research. The high frequency valves (35A series of MAC, USA) are controlled by the PLC (CP1H OMRON) and the position feedback signals from the optical encoder are also sent into the PLC. $P'_{\text{target}}(x, y, z)$, actual needle position, can be achieved by the real time MRI analysis during needle insertion. Potential sources of error in the system are the mechanism manufacturing error, the robot movement control error, soft tissue could be deformed under the tissue-needle interaction and the image based measurement error. Of the above, the $P'_{\text{target}}(x, y, z)$ cannot be the planned $P_{\text{target}}(x, y, z)$. The errors could be fed back to the control system and used as direction of adjusting the needle orientation. Proper precision and good tracking ability could be obtained with this half close loop feedback controller.

3. Kinematic Analysis and Trajectory Planning

3.1. Coordinate system

Coordinate system is established as shown in Fig. 4. Four slider-guide mechanisms at pitch/lift module are simplified into two, for each cylinder at bottom stage drives a pair of this mechanism simultaneously.

The coordinate system fixed on the pitch/lift module is O-xyz, and the origin is at the center of front joint at bottom board. Positive direction of axis *y* is perpendicular to the guide at bottom. Positive direction of axis *z* is upward vertically. Axis *x* is determined by right-hand rule.
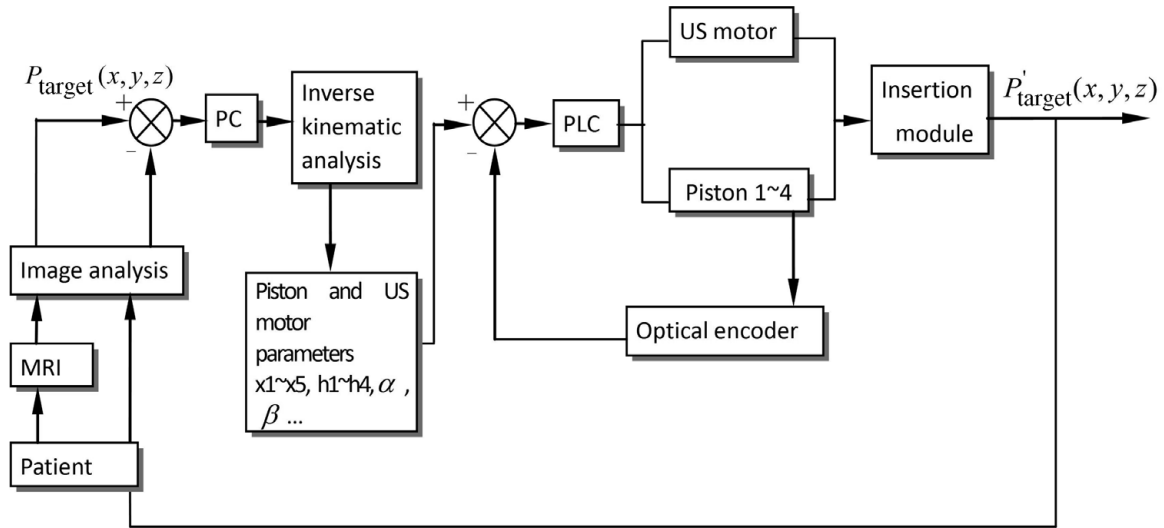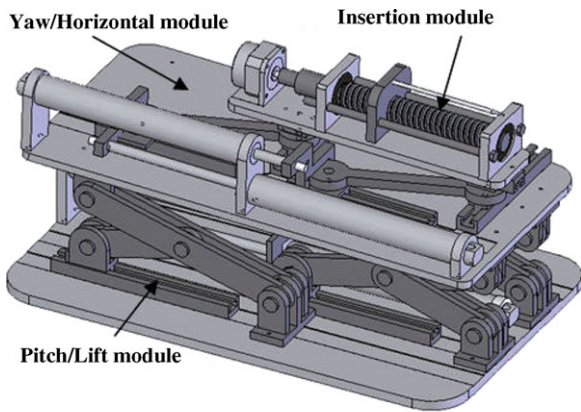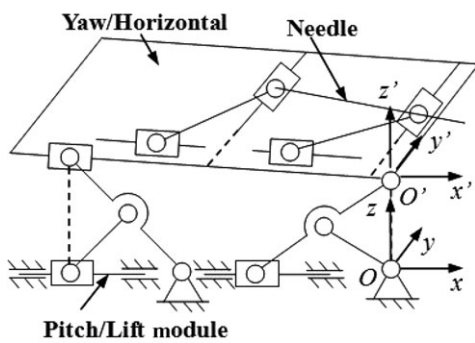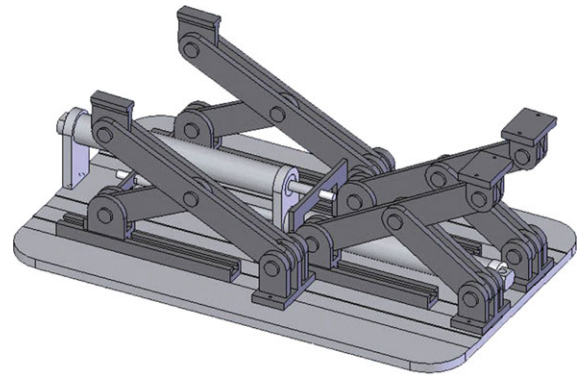
Fig. 3. Equivalent diagram of control system.

(a)

(b)

Fig. 4. (Colour online) 3D model and equivalent kinematic diagram of the robotic system (a) 3D model; (b) Kinematic diagram.
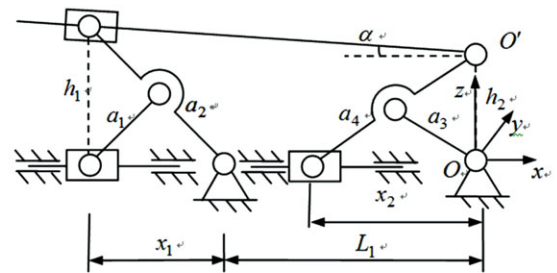

(a)

(b)

Fig. 5. (Colour online) 3D model and equivalent kinematic diagram of pitch/lift module (a) 3D model; (b) Kinematic diagram.

3.2. Forward kinematics analysis

The objective of forward kinematics analysis for this hybrid-driven robot is intended to compute the corresponding end effector's pose and find out the mechanism workspace.

Pitch/lift module equivalent kinematic diagram is shown in Fig. 5. Two mechanisms moving synchronously and asynchronously cause lift and pitch motion. In our prototype, a_1, a_2, a_3, a_4 are the length of rods; h_1, h_2 are the height motion range of the end-effecter; x_1, x_2 are the

distance between sliders and the hinge joints at bottom stage respectively; and α is the pitch angle of the mid stage, which ultimately influences the needle pitch angle.

From Fig. 5, h_1 and h_2 can be deduced as following:

$$h_1 = 2\sqrt{a^2 - \left(\frac{x_1}{2}\right)^2} \tag{1}$$

$$h_2 = 2\sqrt{a^2 - \left(\frac{x_2}{2}\right)^2} \tag{2}$$

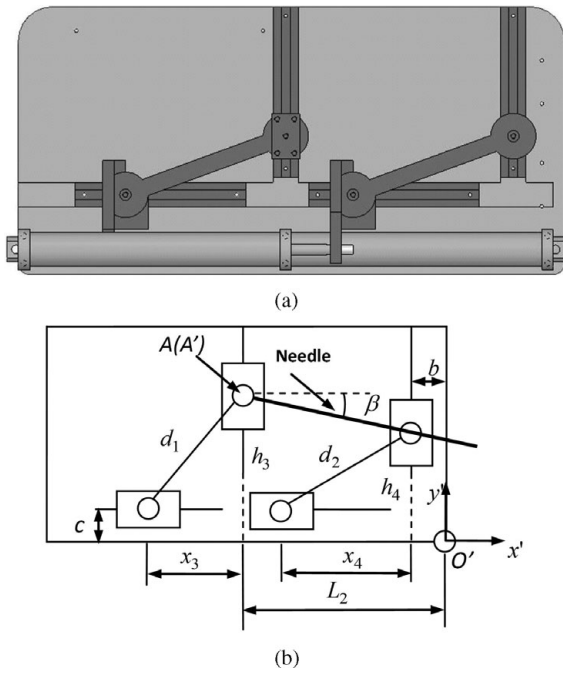where $a_1 = a_3 = a$, $a_2 = a_4 = 2a$.

(a)

(b)

Fig. 6. 3D model and equivalent kinematic diagram of yaw/horizontal module (a) 3D model; (b) kinematic diagram.

The mid stage is lifted by these two mechanisms at bottom; so, the angle α between bottom and mid stage is:

$$\alpha = \text{arctg} \frac{h_2 - h_1}{L_1 + x_1} \tag{3}$$

where L_1 is the distance between two joints at bottom stage. When $h_2 > h_1$, α is positive.

From the deduction above, the orientation of mid stage can be received. Accordingly, the coordinate of $O'(0, 0, h_2)$ is obtained, which is considered as the referenced coordinate system origin of mid stage.

The equivalent kinematic diagram of yaw/horizontal module is shown in Fig. 6. In this module, d_1, d_2 are the length of rods; x_3, x_4 are the movement distance; and β is the yaw angle of the needle. When two pistons move at x' direction simultaneously, the needle performs a horizontal movement; when they move asynchronously, yaw motion is performed.

From Fig. 6; h_3, h_4 can be deduced as following:

$$h_3 = \sqrt{d^2 - x_3^2} \tag{4}$$

$$h_4 = \sqrt{d^2 - x_4^2} \tag{5}$$

Where $d_1 = d_2 = d$.

The yaw angle of needle is

$$\beta = \text{arctg} \frac{h_4 - h_3}{L_2 - b} \tag{6}$$

Where L_2 is the distance between the coordinate system origin and the left guide, when $h_4 > h_3$, β is positive.

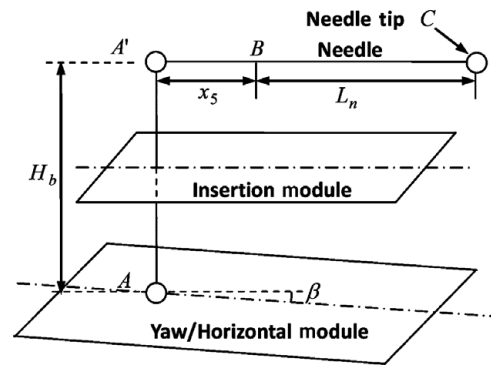This stage is used for adjusting the yaw angle and needle position in y direction. From the deduction above, needle

orientation could be completed. The coordinate of point A is obtained as follows:

$$\begin{bmatrix} x_A \\ y_A \\ z_A \end{bmatrix} = \begin{bmatrix} -L_2 \cos \alpha - H_a \sin \alpha \\ c + h_3 \\ h_2 - L_2 \sin \alpha + H_a \cos \alpha \end{bmatrix} \tag{7}$$

Where H_a is a parameter to correct height error created by the thickness of mid stage board.

Point A' is on the top of point A, and is figured as origin of needle. The equivalent kinematic diagram of insertion module is shown in Fig. 7. H_b is the distance between A' and A; x_5 is the displacement actuated by ultrasound motor; and L_n is the length of needle.

From Fig. 7, the coordinate of point C is obtained as follow:

$$\begin{bmatrix} x_C \\ y_C \\ z_C \end{bmatrix} = \begin{bmatrix} (x_5 + L_n) \cos \alpha \cos \beta - L_2 \cos \alpha - H \sin \alpha \\ (x_5 + L_n) \sin \beta + c + h_3 \\ (x_5 + L_n) \sin \alpha \cos \beta + h_2 - L_2 \sin \alpha + H \cos \alpha \end{bmatrix} \tag{8}$$

Where $H = H_a + H_b$.

The coordinate of $C(x_C, y_C, z_C)$, pitch angle α, and yaw angle β define the position and posture of the needle. Every array $(x_1, x_2, x_3, x_4, x_5)$ can determine the only one position of needle tip and posture of its body.

According to the requirements of brachytherapy and actual size of prostate, robot workspace should be larger than the prostate, and the patient body and MRI scanner bore should not be intervened. Workspace is calculated to verify the working ability of this hybrid-driven robot from geometric perspective.

Parameters of this 5-DOF hybrid-driven robot are shown in Table I.

For the limitation of actuator design and dimension, motion ranges of actuators are shown in Table II.

Fig. 7. Equivalent kinematic diagram of insertion module.

Table I. Parameters of robot.

	a_1	a_2	a_3	a_4	b	c	d_1
Length (mm)	105	210	105	210	25	–7.5	150
	d_2	H_a	H_b	H	L_n	L_1	L_2
Length (mm)	150	100	65	165	150	192	225

Table II. Motion ranges of actuators.

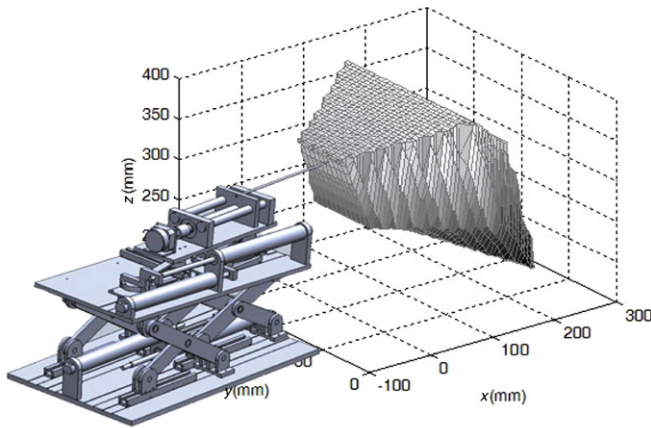|	Range of motion (mm)	DOF
x_1	[110, 250]	Pitch/Lift
x_2	[110, 250]	
x_3	[45, 120]	Yaw/Horizontal
x_4	[45, 120]	
x_5	[90, 240]	Insertion

Fig. 8. (Colour online) Workspace of robot.

With the parameters listed in Table I and the motion ranges listed in Table II, ultimate value of the reachable points in space can be calculated. And then, workspace of the robot is obtained, as shown in Fig. 8.

The workspace contains all the points that the needle tip can reach. The size of workspace is larger than $200 \times 80 \times 150 \, \text{mm}^3$. According to the design requirements, this robot configuration can fulfill the limitation of the MR core space and the distance between patient legs as shown in Fig. 1. Compared with the prostate size that is about $20 \times 30 \times 40 \, \text{mm}^3$, the workspace is enough. The robot is able to perform the surgery from geometric perspective.

3.3. Inverse kinematics analysis

The inverse kinematics of this hybrid driven robot is to solve the cylinder pistons motion (x_1, x_2, x_3, x_4) and ultrasonic motor motion x_5 by the given body posture and tip position of needle. Before the needle insertion, a trajectory optimization will be planned, which contains insertion point in the area of perineum and insertion angle toward the target. Additionally, forces load on tip of needle will deform the soft tissue and displace the targeted seed positions.[19] For the reasons mentioned above, the adjustment of the needle orientation and insertion during brachytherapy is the precondition of an ideal surgery.

Assume that needle tip point C_{n-1} is at $(x_{Cn-1}, y_{Cn-1}, z_{Cn-1})$ and next target point C_n is at (x_{Cn}, y_{Cn}, z_{Cn}), as shown in Fig. 9. When the needle is located in $B_{n-1}C_{n-1}$ position, we define α_{n-1} is the pitch angle of the mid stage and β_{n-1} is the yaw angle of the needle. Likewise, α_n and β_n are the corresponding angle of the needle that is in the posture of B_nC_n, as shown in Fig. 10. The $B_{n-1}C_{n-1}$ is the current posture of needle and B_nC_n is the next posture for needle. To
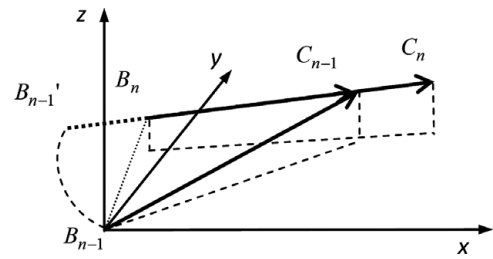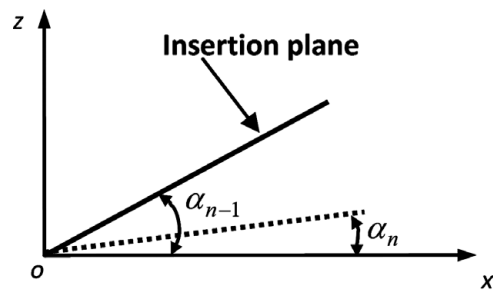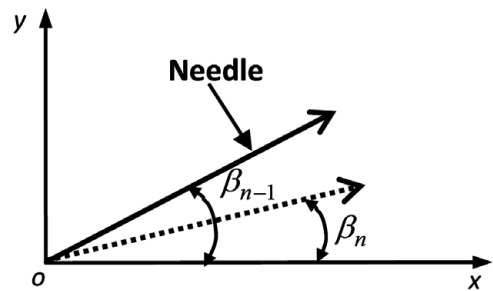

Fig. 9. Insertion procedure diagram of two discretized points C_n and C_{n-1} (a) Front view; (b) Top view.

Fig. 10. α and β of two discretized points C_n and C_{n-1}.

avoid stabbing obstacles, a rotation around needle tip C_{n-1} is performed during insertion along line $C_{n-1}C_n$.

Points $C_n(x_n, y_n, z_n)$ and $C_{n-1}(x_{n-1}, y_{n-1}, z_{n-1})$ are preplanned before the needle insertion, so, they are considered as known conditions. When the needle change from the posture of $B_{n-1}C_{n-1}$ to the posture of B_nC_n, α_n, and β_n can be obtained as following:

$$\alpha_n = \text{arctg} \frac{z_n - z_{n-1}}{x_n - x_{n-1}} \tag{9}$$

$$\beta_n = \text{arctg} \frac{y_n - y_{n-1}}{\sqrt{(z_n - z_{n-1})^2 + (x_n - x_{n-1})^2}} \tag{10}$$

We assume that B_0C_0 is the initial posture of needle and the needle tip is at point $C_0(x_0, y_0, z_0)$. And then, the pitch angle of the mid stage and the yaw angle of the needle is α_0 and β_0. Point $C_0(x_0, y_0, z_0)$, α_0, and β_0 are the initial conditions, so, they are considered as known. According to Eqs. (9) and (10) and the coordinate points of $c_0, c_1, c_2 \ldots c_n, \alpha_1, \alpha_2 \ldots \alpha_n$ and $\beta_1, \beta_2 \ldots \beta_n$ can be obtained.

We define $x_{in}(i = 1, \ldots, 5)$ are the value of x_i that are the pistons movement distance, have been mentioned before. From the coordinate of point C_n, according to Eqs. (2), (4)–(6), and (8), $(x_{1n}, x_{2n}, x_{3n}, x_{4n}, x_{5n})$ at α_n, β_n, and

$C_n(x_{Cn}, y_{Cn}, z_{Cn})$ are obtained as follows:

$$x_{2n} = \sqrt{4a^2 - \left[z_{Cn} + L_2\sin\alpha_n - H\cos\alpha_n - \left(\frac{x_{Cn} + L_2\cos\alpha_n + H\sin\alpha_n}{\cos\alpha_n}\right)\sin\alpha_n\right]^2} \tag{11}$$

$$x_{3n} = \sqrt{d^2 - \left[y_{Cn} - c - \left(\frac{x_{Cn} + L_2\cos\alpha_n + H\sin\alpha_n}{\cos\alpha_n\cos\beta_n}\right)\sin\beta_n\right]^2} \tag{12}$$

$$x_{4n} = \sqrt{d^2 - \left[(L_2 - b)\tan\beta_n - y_{Cn} + c + \left(\frac{x_{Cn} + L_2\cos\alpha_n + H\sin\alpha_n}{\cos\alpha_n\cos\beta_n}\right)\sin\beta_n\right]^2} \tag{13}$$

$$x_{5n} = \frac{x_{Cn} + L_2\cos\alpha_n + H\sin\alpha_n}{\cos\alpha_n\cos\beta_n} - L_n \tag{14}$$

where x_{1n} can be obtained from the equation below:

$$(L_1 + x_1)\tan\alpha_n = 2\sqrt{a^2 - \frac{x_2^2}{4}} - 2\sqrt{a^2 - \frac{x_1^2}{4}} \tag{15}$$

So that,

$$x_{1n} = \frac{-B + \sqrt{B^2 - 4AC}}{2A} \tag{16}$$

Where

$$A = \tan^2\alpha_n + 1 \tag{17}$$

$$B = 2L_1\tan^2\alpha_n - 2h_2\tan\alpha_n \tag{18}$$

$$C = h_2^2 + L_1^2\tan^2\alpha_n - 2h_2L_1\tan\alpha_n - 4a^2 \tag{19}$$

With the deduced result of $(x_{1n}, x_{2n}, x_{3n}, x_{4n}, x_{5n})$ at α_n, β_n, and $C_n(x_{Cn}, y_{Cn}, z_{Cn})$, the piston extended length can be known. After these results are inputted into the kinematic control system, the needle can be steered to the target point as planned.

4. Kinematic Simulation

During brachytherapy, soft-tissue deformation occurring during the pre-rupture and insertion phases can result in the needle missing its intended target. In this procedure, target point is the position that radioactive seeds or medicine should be placed in or around the tumor, and the obstacle objects are the important tube, blood vessel that cannot be punctured. Examination of the results from an experienced physician injecting seeds into 20 patients showed average displacement errors of 0.47 cm in depth and 0.22 cm in height, yielding an average placement error of 0.63 cm that corresponds to 21% of the average prostate diameter (3 cm).[20,21] The incorporation of dynamic trajectory corrections at each time step is therefore essential for the needle to reach its target destination and effectively increase implant precision.
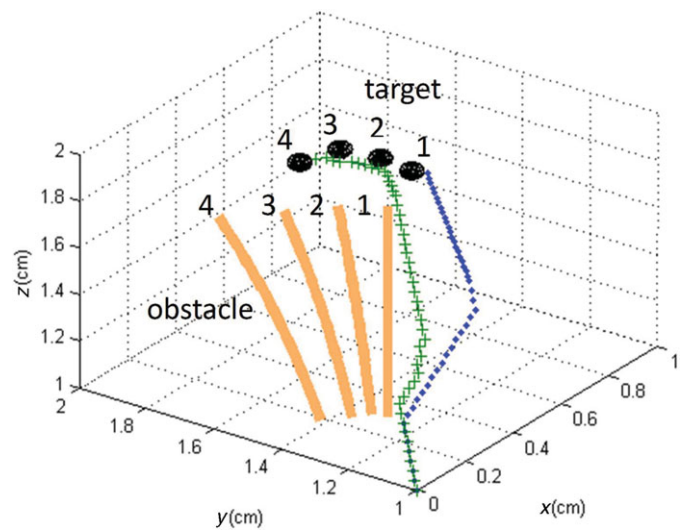

Fig. 11. (Colour online) 3D dynamic trajectory planning result, four positions of target movement as well as obstacles to be avoided by the needle.

In this research, 3D dynamic trajectory planning algorithm and a Mooney–Rivlin material model are adopted.[22] The result is shown in Fig. 11, where the orange cylinder is the obstacle that represents the important tube, nerve, or artery embedded in the soft tissue, and the numbers 1, 2, 3, and 4 represent the cylinder positions and deformation status of the four adjacent time steps. The black sphere is the target to be reached by the needle, and the numbers 1, 2, 3, and 4 represent the target positions at each time step. The blue path is the trajectory planning result before deformation. The green path is the dynamic trajectory planning result. Without dynamic trajectory planning, the needle would be inserted into the tissue at target location 1. However, the tissue deforms during insertion, causing the target to move to location 4 and yielding an insertion error equal to the distance between location 4 and location 1. With dynamic trajectory planning, the needle would be inserted into the target position along the green path and successfully reached at position 4. During the insertion, as sharp changes occurred in the path, the needle is moved along the inscribed arc of the two intersecting line paths.

We assume that an obstacle is just between the insertion point and target point. A trajectory had been planned to avoid obstacle and reach the target, as shown in Fig. 12. The arrows present the direction of minimal potential field. The black line is the insertion trace that needle should be steered.

Assume that insertion point is at (0, 128, 196), target point at (50, 130, 200) with a ball with radius 2 mm. Obstacle is generated as a cylinder with radius 1 mm through point (40, 129, 200). The optimized trajectory is around the obstacle and along with the direction of artificial potential field, however, limited by the robot kinematic characteristic and prostate needle insertion surgery method, range of α and β should be between ±15°. Especially, in the surgery, the range of angle is usually less than ±10°.

The trajectory is discretized into points. Bring the coordinate of discrete points into Eqs. (11)–(19), pistons
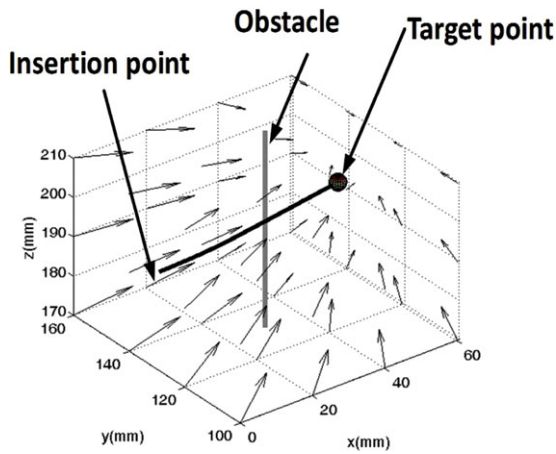
Fig. 12. (Colour online) Pre-planned optimized trajectory.

movement distance can be calculated as shown in Fig. 13(a)–(c) and the needle can be steered to move along the trajectory. At the beginning of insertion, the artificial potential field interact the needle and drives it escape from the obstacle. After a distance of insertion, the interaction of target point is reinforced, and gradually transforms into the main force. Then, the needle rotates and inserts toward target point.
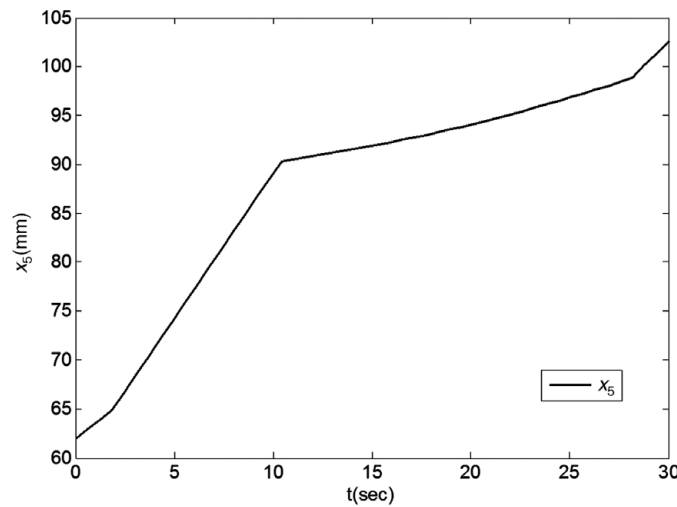
5. Experiment

In order to evaluate the robot mechanism behavior accuracy objectively and exclude the errors brought by registration, image distortion, etc., a vision based setup is built up in the lab as shown in Fig. 14(a) and (b). The phantom is made of PVA hydrogel, and the material of puncture needle (Invivo, 150 mm, 18G) is titanium. Two high speed cameras (Basler Scount), which are fixed at the horizontal plane and the vertical plane, are used to acquire real-time images of the needlepoint. The acquired images are then transmitted to a computer to acquire the real position through a digital video interface card (Matrox concord), which has an IEEE 1394b adaptor. Experiment has been divided into two parts. One is the system calibration and another is the needle tip position precision evaluation.
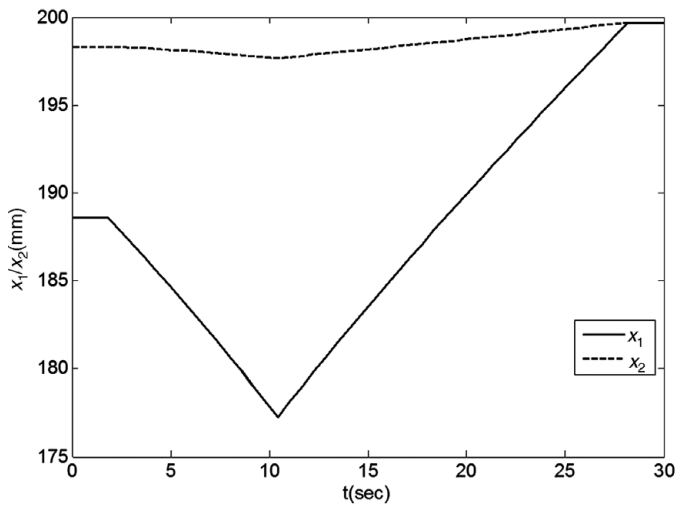

(a)
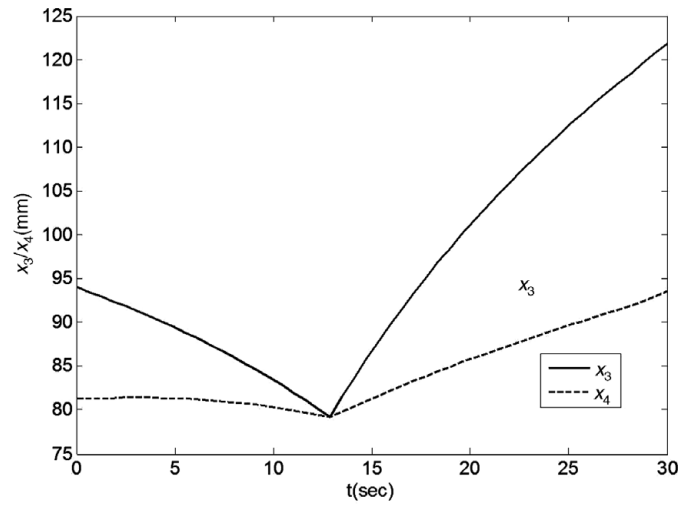
(b)

(c)

Fig. 13. Movement of actuators to achieve pre-planned motions (a) Displacement of x_1 and x_2; (b) Displacement of x_3 and x_4; (c) Displacement of x_5.
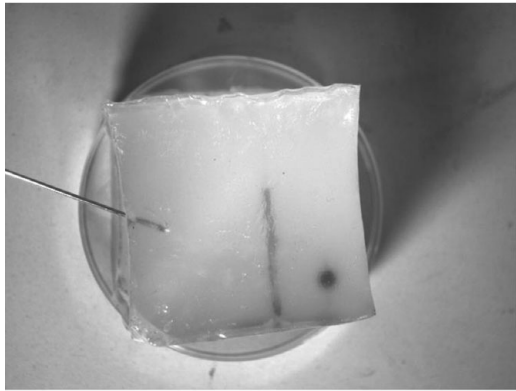
Table III. Experiments data.

	1	2	3	4	5	6	7	8	9	Actual coordinate	Average coordinate
x	102.4	102.6	102.6	102.7	102.2	102.3	102.8	102.6	102.7	102	102.54
y	135.2	135.4	135.4	135.6	135.8	135.6	135.7	135.1	135.9	135	135.52
z	310.5	310.8	310.6	310.8	310.7	310.2	310.2	310.6	310.2	310	310.51
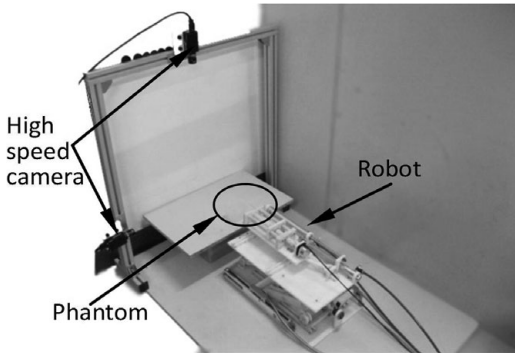
(a)

(b)

Fig. 14. Precision experiment setup based on image acquisition (a) Vision based experiment setup; (b) Local enlarged phantom image.

The purpose of the system calibration is to acquire relationship of pixel coordinates and spatial coordinates of the target point. And the precision of the visual system is depended on the precision of system calibration. Firstly, establish the imaging model of camera and the relevant coordinate system, then, the relational model of spatial point in imaging coordinate system and space coordinate system are obtained. Secondly, gather the template images with various gestures and calculate the unit matrix between template plane and template image. Finally, the internal and external parameters of camera can be gained with unit matrix and the constraint equation of relevant parameters. The error model is established, and the full camera parameters are gained after errors corrected.

The most common pinhole camera model is established as the camera model and the coordinate system is set up as shown in Fig. 15.

In order to evaluate precision of the system calibration, the results of calibration are used to recover the world coordinate of feature point. Compared the recovered coordinate with the
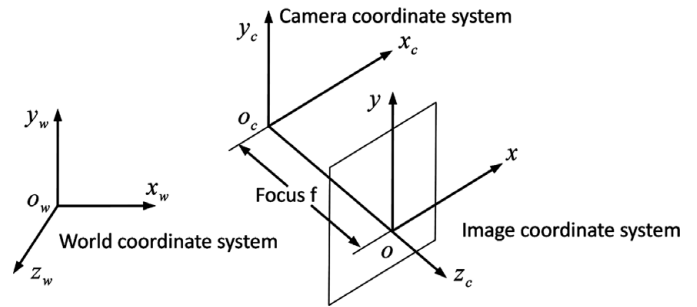

Fig. 15. The pinhole camera model.

actual world coordinate, the calibration precision of camera is obtained. The maximum error of system calibration is 0.034 mm in x direction, 0.038 mm in y direction and 0.03 mm in z direction.

For a target point, several needle insertion experiments are operated to verify the performance of the robotic system, and then, the actual position of the needlepoint is obtained and the results are shown in Table III.

The needle body has some deflection in those needle insertion experiments, and this is the major reason that leads to errors. The equation to evaluate the precision of needle tip point is shown as follows:

$$p = \sqrt{(x - \bar{x})^2 + (y - \bar{y})^2 + (z - \bar{z})^2} \quad (20)$$

With the image processing results and according to Eq. (20), we obtained the precision of the needle tip point is 0.9 mm.

6. Conclusion

This paper analyzes the mechanism design of a 5-DOF hybrid-driven prostate needle insertion robot, which consists of pitch/lift module, yaw/horizontal module, and insertion module. These modules are structured by parallel mechanism, and linked by serial mechanism. The first prototype is being built by Tianjin University. The design of robot is well adaptive to the prostate needle insertion surgery according to the workspace and motion requirement. The geometry analysis is employed for the forward kinematics of robot. With the dynamic trajectory optimization principle, inverse kinematics is deduced. An optimized trajectory is simulated and achieved control parameters with inverse kinematics. Additionally, the robot performance of control and accuracy are being tested in the lab.

As the result of forward kinematics analysis shown, the robot workspace is larger than needed. In the future, the configuration of this robot should be optimized and the volume of it can be reduced.

Acknowledgments

Competing Interests

The authors declare that they have no competing interests.

References

1. A. Jemal, R. Siegel, E. Ward, Y. P. Hao, J. Q. Xu and M. J. Thun, "Cancer statistics," *CA Cancer J. Clin.* **59**, 225–249 (2009).
2. A. Tornes and M. Eriksen, "A new brachytherapy seed design for improved ultrasound visualisation," *Ultrasonics* **2**, 1278–1283 (2009).
3. S. Jiang, N. Hata and R. Kikinis, "Needle Insertion Simulation for Image-Guided Brachytherapy of Prostate Cancer," *International Conference of Bioinformatics Biomedical Engineering, iCBBE* (2008) pp. 1682–1685.
4. A. Krieger, R. C. Susil, C. Menard, G. Fichtinger, E. Atalar and L. Whitcomb, "Design of a novel MRI compatible manipulator for image guided prostate interventions," *IEEE Trans. Biomed. Eng.* **52**(2), 306–313 (2005).
5. L. Y. Lin, R. R. Patel, B. R. Thomadsen and D. L. Henderson, "The use of directional interstitial sources to improve dosimetry in breast brachytherapy," *Med. Phys.* **35**(1), 240–247 (2008).
6. M. A. Meltsner, Design and Optimization of a Brachytherapy Robot *Ph.D. Dissertation* (Madison, WI: University of Wisconsin, 2007).
7. C. S. Shiow, C. C. Huang and C. S. Chen, "Development of image-guided robotic system for surgical positioning and drilling," *Robotica* **55**, 375–383 (2007).
8. J. S. Dai, "Surgical robotics and its development and progress," *Robotica* **28**, 161 (2010).
9. A. A. Goldenberg, J. Trachtenberg, Y. Yi, R. Weersink, M. S. Sussman, M. Haider, L. Ma and W. Kucharczyk, "Robot-assisted MRI-guided prostatic interventions," *Robotica* **28**, 215–234 (2010).
10. D. Liu, T. M. Wang, C. Tang and F. Zhang, "A hybrid robot system for CT-guided surgery," *Robotica* **28**, 253–258 (2010).
11. Q. Huang, G. B. Bian, X. G. Duan, H. H. Zhao and P. Liang, "An ultrasound-directed robotic system for microwave ablation of liver cancer," *Robotica* **28**, 209–214 (2010).
12. H. Bassan, T. Hayes, R. V. Patel and M. Moallem, "A Novel Manipulator for 3D Ultrasound Guided Percutaneous Needle Insertion," *Proceedings of IEEE International Conference on Robotic and Automation*, Roma, Italy (2007) pp. 617–622.
13. S. E. Salcudean, T. D. Prananta, W. J. Morris and I. Spadinger, "A Robotic Needle Guide for Prostate Brachytherapy," *Proceedings of IEEE International Conference on Robotics and Automation*, Pasadena, CA (2008) pp. 2975–2981.
14. Y. Yu, T. Podder, Y. D. Zhang, W S. Ng, V. Misic, J. Sherman, L. Fu, D. Fuller, D. J. Rubens, J. D. Strang, R. A. Brasacchio and E. M. Messing, "Robot-assisted prostate brachytherapy," *Med. Image Comput. Comput. Assist. Interv.* **9**(1), 41–49 (2007).
15. K. K. Yu and H. Hricak, "Imaging prostate cancer," *Radiol. Clin. North Am.* **38**(1), 59–85 (2000).
16. D. Stoianovici, D. Song, D. Petrisor, D. Ursu, D. Mazilu, M. Mutener, M. Schar and A. Patriciu, "MRI stealth robot for prostate interventions," *Minim. Invasive Ther.* **16**(4), 241–248 (2007).
17. G. S. Fischer, J. Iordachita and G. Fichtinger, "Design of a robot for transperineal prostate needle placement in MRI scanner," *Mechatronics Conference on Digital Object Identifier* (2006) pp. 592–597.
18. S. E. Song, N. B. Cho, G. Fischer, N. Hata, C. Tempany, G. Fichtinger and I. Iordachita, "Development of a pneumatic robot for MRI-guided transperineal prostate biopsy and brachytherapy: New approaches," *IEEE International Conference on Robotics and Automation*, Anchorage, Alaska, USA (2010) pp. 2580–2585.
19. S. Haker, R. V. Mulkem, J. R. Roebuck, J. R. Roebuck, A. S. Barnes, S. DiMaio, N. Hata and C. Tempany, "Magnetic resonance-guided prostate interventions," *J. Magn. Reson. Imaging* **16**, 355–682 (2005).
20. R. Taschereau, J. Pouliot, T. Jean and D. Tremblay, "Seed misplacement and stabilizing needles in transperineal permanent prostate implants," *Radiother. Oncol.* **55**, 593–631 (2000).
21. R. Alterovitz, K. Y Goldberg, J Pouliot and I. C. Hsu "Sensorless planning for medical needle insertion in deformable tissues," *IEEE T Inf. Technol. B* **13**(2), 217–225 (2009).
22. S. Jiang, X. Y. Liu and Y. C. Song, "3D Trajectory Planning Based on FEM with Application of Brachytherapy," *Proceedings of International Conference Biomedical Engineering Informatics, BMEI,* Tianjin, China (2009) pp. 1–5.